Interface Morphology Description and Quantification of Al–Cu Magnetic Pulse Welding Joints Using X-Ray Micro-computed Tomography

Benjamin Zielinski, Tarik Sadat, Robin Guibert, Denis Jouaffre, Eric Markiewicz, Laurent Dubar

▶ **To cite this version:**

Benjamin Zielinski, Tarik Sadat, Robin Guibert, Denis Jouaffre, Eric Markiewicz, et al.. Interface Morphology Description and Quantification of Al–Cu Magnetic Pulse Welding Joints Using X-Ray Micro-computed Tomography. Journal of Nondestructive Evaluation, 2023, 42 (3), pp.72. 10.1007/s10921-023-00984-4 . hal-04208963

HAL Id: hal-04208963
https://uphf.hal.science/hal-04208963v1

Submitted on 15 Sep 2023

HAL is a multi-disciplinary open access archive for the deposit and dissemination of scientific research documents, whether they are published or not. The documents may come from teaching and research institutions in France or abroad, or from public or private research centers.

L'archive ouverte pluridisciplinaire **HAL**, est destinée au dépôt et à la diffusion de documents scientifiques de niveau recherche, publiés ou non, émanant des établissements d'enseignement et de recherche français ou étrangers, des laboratoires publics ou privés.

Distributed under a Creative Commons Attribution - NonCommercial - ShareAlike 4.0 International License

Interface morphology description and quantification of Al-Cu Magnetic Pulse Welding joints using X-ray micro-computed tomography

Benjamin Zielinski,[1,2*], Tarik Sadat[1], Robin Guibert[1], Denis Jouaffre[3], Eric Markiewicz[1], Laurent Dubar[1]

[1]Univ. Polytechnique Hauts-de-France, CNRS, UMR 8201 - LAMIH, F-59313, Valenciennes, France.
[2]INSA Hauts-de-France, F-59313, Valenciennes, France.
[3]PFT Innovaltech - Lycée Condorcet, Saint-Quentin, 02100, France.

*Corresponding author(s). E-mail(s): benjamin.zielinski@outlook.com;

Abstract

Magnetic pulse welding (MPW) is a relatively new welding technique that has been gaining increasing attention from various industries. MPW allows for the welding of dissimilar materials, such as aluminum and copper, but with specific features at the interface. This study proposes the use of an original approach based on X-ray micro-computed tomography (XCT) to probe and analyze the surface interface between two dissimilar welded components. This method does not require the use of a peeling test to reveal the interface welding. X-ray micro-computed tomography enables a global analysis of the interface and highlights specific features of MPW, such as vortexes and waves, from a new perspective involving metrics.

Two vortex morphologies were observed at the interface and were described as standard or broken vortexes. They were classified based on their morphologies, sizes, and densities. Waves and vortexes were found to be inhomogeneous along the length and width of the welding direction at the interface, with sizes that could triple depending on the localization. The surfaces at the interface were numerically extracted and evaluated using roughness parameters. These values represent an increase in the average contact surface area of more than 26% between the two welded components.

Vortex features obtained from the XCT analysis were similar to those observed on cross-sectional optical or electronic images, but containing lateral information

(creation and collapsing) that are not available with standard cross-sectional images. These results demonstrate the material interlocking at the interface between the materials.

Keywords: Magnetic pulse welding, X-ray computed tomography, Interface, Morphology, Copper, Aluminum

1 Introduction

In our world, every system or tool is an assembly of several components with different sizes and characteristics. Various processes are available for assembling these different components, depending on their natural constitutive materials and functions. Welding processes and others techniques, such as bolts/nuts, crimping, or rivet techniques are commonly used to produce assemblies. Welded parts can be used for electrical connections between two elements, as structural bonds, or to constrict leaks.

Multiple methods exist to weld parts, they can be classified as unconventional or conventional welding processes, such as metal inert gas (MIG) or tungsten inert gas (TIG). In these instances, the pieces are heated to the melting points of the parts or the metal filler. Conventional welding techniques can produce noxious fumes and gases. These gases and fumes affect the health of workers, and exposure to welding fumes can create persistent pulmonary bronchitis [3].

The concept is different for unconventional techniques and is based on other physical phenomena. Electromagnetic pulse welding (EMPW), also known as Magnetic pulse welding (MPW) is one such technique. This method is based on severe plastic deformation ([42]) and can reduce the formation of intermetallic compounds (IMC) during the welding of dissimilar materials such as aluminum (Al) and copper (Cu) ([27]). Al/Cu IMCs have a negative impact on the electrical properties of the joints due to their worse electrical conductivity compared to aluminum and copper [35] and should be avoided.

MPW uses electricity as a power source for the welding process [40], making it environmentally sustainable ([14]). MPW also has the advantage of not producing toxic fumes, thereby reducing the risk of health issues for workers.

MPW was described as high-velocity impact welding (HVIW) or solid-state welding [24]. These denominations are linked to the process conditions during welding and the quality of the produced seam. Typically, the collision speed is in the range of $200 - 500$ m/s [42] and experimentally confirmed by other researchers ([12, 16]). Welding windows can be produced to depict the most appropriate conditions for the welding, as done for Al/Cu assemblies [43]. Al/Cu assemblies can combine the lightweight nature of aluminum with the high electrical and thermal conductivity of copper. Such structures are commonly utilized in power transmission, heat exchanger tubes, and electrical connectors[35].

The classification of MPW as a solid-state welding method is owing to its ability to produce a minimal heat-affected zone, and a limited diffusion zone along the weld joint resulting in low average temperatures of the parts post-welding ([33]). MPW can

provide linear or circular welds and is considered as fast, reliable, and cost-effective [36]. It is possible to achieve high-quality tubular joints without helium gas leakages [29].

MPW and other HVIW techniques (Explosive Welding (EXW) [1], Laser Impact Welding (LIW)[9], and Vaporizing Foil Actuator Welding (VFAW) [22]) have commons distinctive features which produce specific morphologies at the interface of the welded elements ([18, 38]).

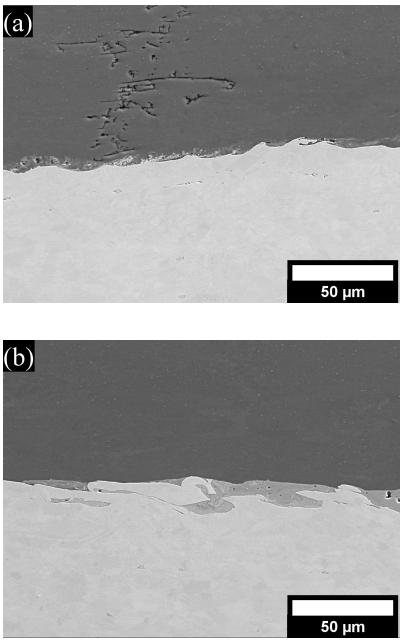

Figure 1: Morphology examples of Al/Cu interface MPW joint - obtained by scanning electron microscopy (SEM) (aluminum on top and copper on bottom in each picture) -(a) Planar and wavy interface morphology example for Al/Cu welded sample - (b) Vortex interface morphology example for Al/Cu welded sample

Figure 1 shows examples of these different morphologies such as the waves or vortexes present on the same welding joint. Researchers have investigated the formation mechanism of these elements experimentally ([6]) or numerically ([23]) in MPW or other HVIW processes. The feature formations were reported to be based on a Kelvin-Helmholtz instability mechanism with shock-wave interactions.

However, the measurements and descriptions of these elements are primarily based on optical or scanning electron microscopy (SEM) images of local sections of the welding seam [34]. The amplitude and periodicity are then measured locally and compared with those of the other joints. This methodology was used to compare numerical and experimental conditions in a recent study [11]. Nonetheless, the measurements were still performed locally and on 2D cross sections of the welding, like this other study

made on aluminum/steel assembly [21] . This strategy was also used to describe the global morphology of the welding interface [17]. However, no information is available regarding the lateral evolution of these features. It was already proved than residual stress in planar magnetic pulse welding is inhomogeneous in the joint [4].

Insufficient research has been conducted on the 3D-study of these morphological features at the interface welding. Recently, X-ray synchrotron micro-tomography was used to show damage at the weld interface after the welding [44]. Also, we note the work done by Lee [15], who used X-ray micro-computed-tomography (µ-CT) to qualitatively observe the interface waves on copper/titanium welding. This approach was interesting but limited to the observation of wave regularity without any quantitative measurements. This study extends the investigation to a new dissimilar material couple, namely, aluminum and copper (Al/Cu), and proposes a methodology to quantitatively describe and measure the features of the welded interface based on the use of µ-CT. Tomography can be used to detect [2] or quantify defects [7] within the material volume.

The main objectives of the study were to use µ-CT to quantitatively measure and describe the surface interface morphology of an Al/Cu dissimilar joint fabricated using MPW. This surface corresponds to the internal interface of the joint between the two dissimilar materials and cannot be reached without employing volume probing techniques such as X-ray µ-CT. In addition, the morphological features (waves and vortexes) on the 3D surface of this interface are not limited by the standard 2D section, which is usually arbitrarily chosen. Subsequently, wave continuity was studied along the width of the joint. Therefore, an automated in-house routine that allows the quantification of the height and periodicity of the features was developed. The results obtained for the Al/Cu samples are presented and analyzed.

2 Methods

2.1 Samples description

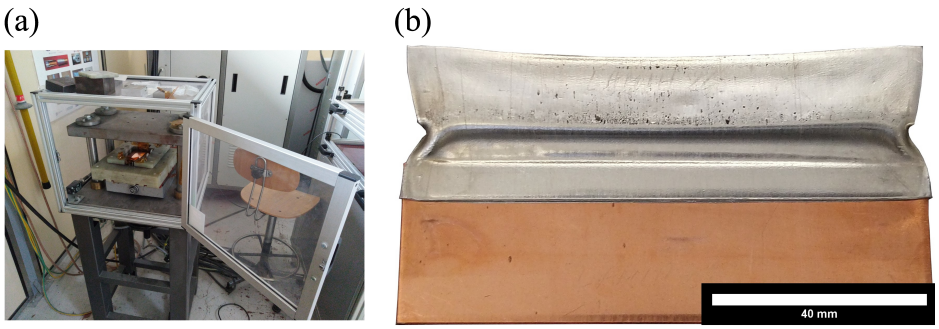

Figure 2: Experimental MPW machine and samples - (a) Setup for the MPW machine - (b) Al/Cu welded joint produced by MPW

Dissimilar Al/Cu joints were manufactured by MPW on a Pulsar 25 kJ-9 kV device with a 690 µF condenser (see Fig. 2-(a)) and an average measured frequency of 17.35 kHz, compared with the theoretical value of 25 kHz at the PFT Innovaltech unit (France) already used previously [26]. Commercial 1050 aluminum sheets with a thickness of 1 mm and commercial copper sheets with a thickness of 2 mm were used. Aluminum was used as the flyer (flying part during the process) and copper as the base metal (fixed position) as displayed in Fig. 3. The other process parameters can be found in Table 1.

The final geometry of the welding is shown in Fig. 2 - (b), and the assembly is approximately 98×53 mm with a welding seam of approximately 90×7 mm in the middle.

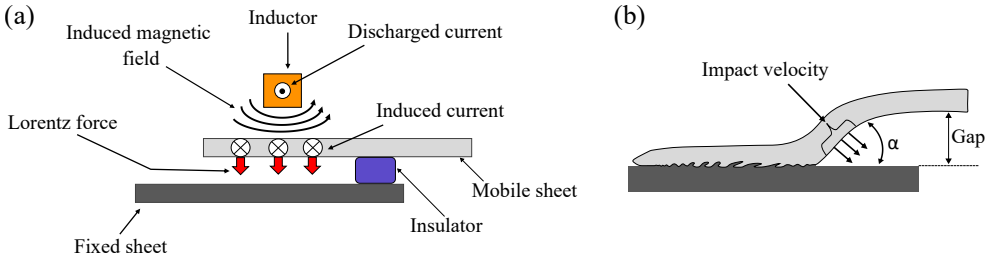

Figure 3: Scheme of the MPW process - (a) Definition of the parts and forces involved during the process - (b) Definition of the main process parameters

Energy (kJ)	Gap (mm)	Overlapping (mm)
19.4	2	7

Table 1: Process parameters for Al/Cu MPW

2.2 X-Ray micro-computed-tomography (µ-CT)

X-Ray µ-CT, also known as X-ray computed-tomography (XCT) technique, can be used to probe the material volume inside a part or an assembly [10] (the welding interface in this work). This method has the advantage of obtaining continuous information about the material without requiring multiple parallel 2D-cross sections.

XCT can be used to measure the interfaces and surfaces ([37]) or pores [41] of parts produced by additive manufacturing. The data can provide a textured surface description, as shown in two studies [30, 31].

However, owing to the global dimensions of the samples and the presence of copper (high X-ray capacity absorption), it was necessary to cut the samples and reduce their size to obtain high-resolution information at the interface. The samples were cut perpendicular to the welding seam with a width of 1.5 mm. Their widths were

reduced by polishing them to less than 1 mm to remove any possible lateral damage to the sample induced by cutting. Final grinding was performed to reduce the copper thickness from 2 mm to 0.5 mm. Three samples were extracted from the original weld and labeled B, C, and D. The samples had a length of 10 mm, width of around 0.8 mm and thickness of 1.5 mm (0.5 mm for the copper and 1 mm for the aluminum). They were located 15, 23, and 31 mm away from the lateral external side of the copper plate.

XCT measurements were performed on the ISIS4D regional platform installed at the University of Lille (France) using an Ultra Tom tomography system (RX Solutions). The parameters used during the scans are listed in Table 2. Tomographic data were reconstructed with a filtered back-projection algorithm using the X-Act software.

Parameter	Unit	Value
Voltage	kV	160
Current	µA	89
Projections number	-	1440
Voxel size	µm	1.69

Table 2: XCT parameters used for Al/Cu samples

2.3 Algorithm and program

Once the data were obtained from XCT, they were treated as gray-level pictures from the 3D volume. A new approach and MATLAB program was developed to extract the interface between two dissimilar materials. The interface surface is a region of interest for MPW welds because of its morphological features (waves and vortexes). The main steps in this program are described in Fig. 4.

The first part of the program (filtering) involved the application of standard filters to the images to remove any remaining noise, adjust the contrast and brightness. A median filter with a kernel size of 3 was used to suppress the salt-and-pepper noise. The image contrast and brightness was reinforced using an unsharp masking filter and histogram adjustment. Once this step was complete, the user defined the interface region to be maintained throughout the following steps. The binarization stage was executed based on automatic Otsu's method [25] and the image was cleaned to remove spurs and H-connection pixels. Finally, all interior pixels were removed to only maintain the external boundary, which was the interface line between the two welded materials. Fig. 5 shows a transformation example for a reduced portion of a tomographic slice into an interface line after the binarization step.

The next step was to transform the pixels interface into an ordered list of points. This list is similar to a mathematical sequence, in which each point corresponds to a coordinate point extracted from the profile. The transformation was performed by converting the pixels interface line into 3D coordinates. The coordinates were obtained from the tomographic section number and interface pixel position. Fig. 6 presents the coordinates base orientation of these interface points compared with the welding geometry. The x-axis represents the welding length interface corresponding to the

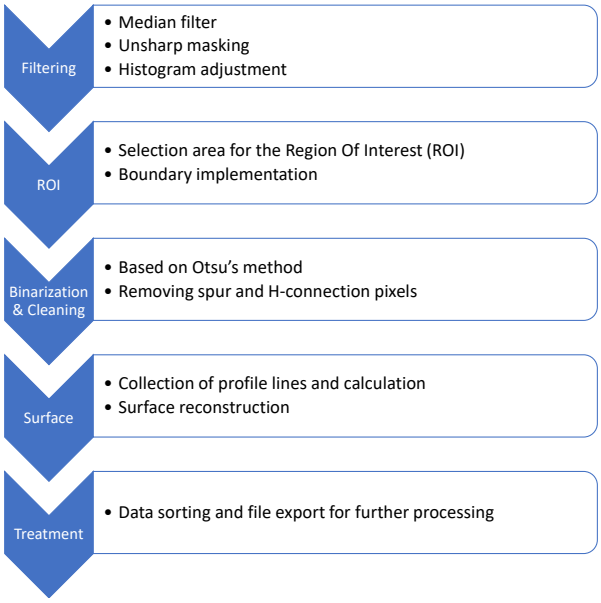

Figure 4: Program workflow for treatment of images

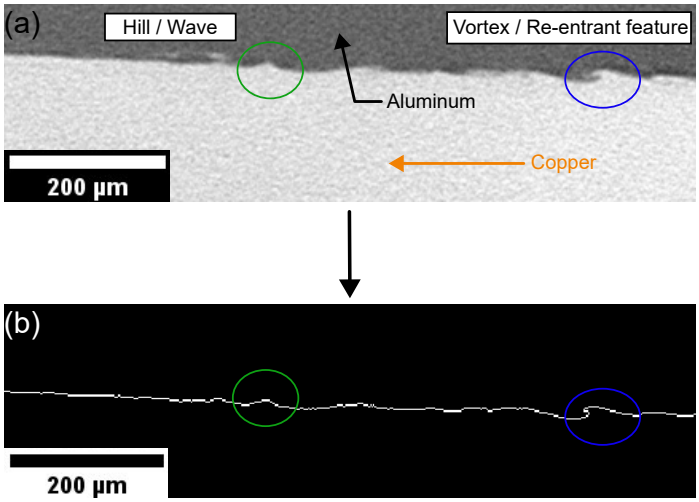

Figure 5: Example of transformed tomographic picture into binarized interface line with specific morphological elements - (a) Initial gray-level picture from X-Ray µ-CT - (b) Binarized interface line

overlapping direction during the welding process. The y-axis shows different tomographic sections corresponding to the assembly width. The z-axis represents the height evolution at the interface.

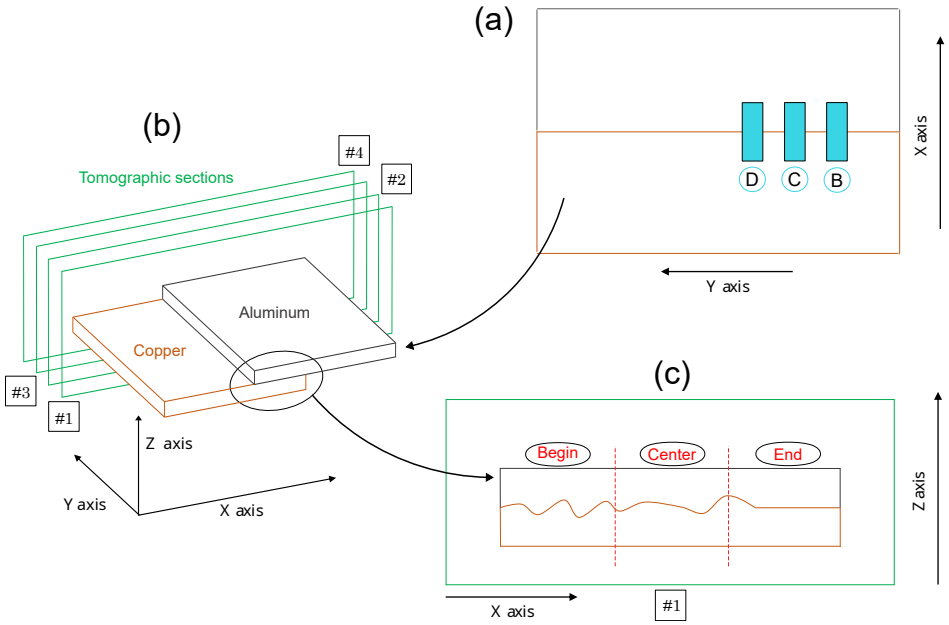

Figure 6: Sample position and coordinates base orientation of welding geometry and tomographic sections -(a) Cross-section sample position on global welding -(b) Tomographic section orientation for sample -(c) Position of different localizations (Begin, Center, End) for sample

Subsequently, the coordinate points were computed in a graph network. Only the points with a Euclidean distance strictly less than two pixels were connected (i.e., points with a lateral or diagonal pixel connection, also called 8-connected pixels). This condition represents the continuity of the interface and allows only necessary connections to be maintained in the graph. The standard points obtained two links (with the previous and subsequent points), whereas the first and last points obtained one link. Some points could obtain three or four connection links, indicating a possible divergence at the interface or uncertain voxel segmentation. When the network graph was completed with all the extracted points from a tomographic section, a shortest path function was used on the graph nodes to remove unnecessary connection links and obtain an ordered list of coordinate points (from the first to the last point). Fig. 7 resumes the graph process to suppress the extra points and order them into a sequence.

This list is now compatible with the use of mathematical functions, such as gradients, to calculate local slopes. The iterative process was performed on all tomographic sections (see Fig. 6).

To summarize the coding work : standard MATLAB functions were used to perform image analysis, but new scripts and methodology were developed to extract, calculate and export the interface surface and its features (waves, vortexes).

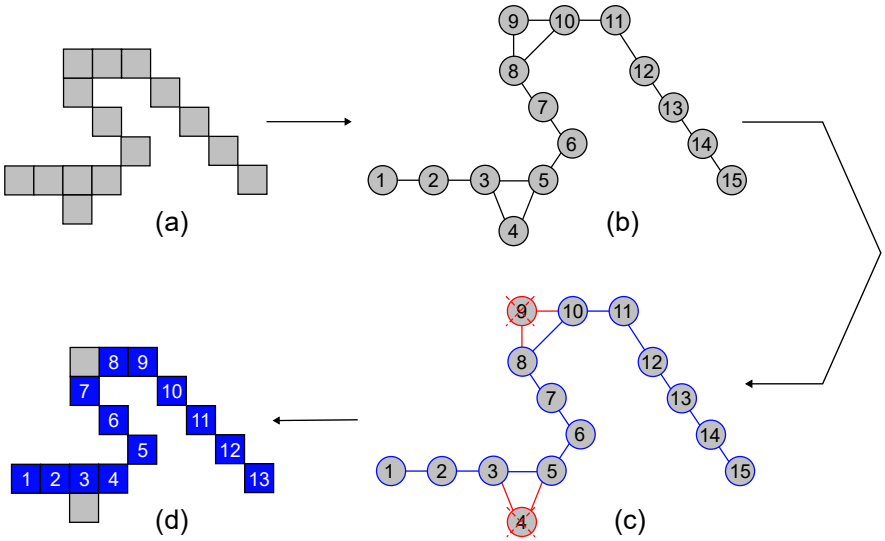

Figure 7: Scheme for presentation of graph network sequence - (a) Initial data input - (b) Graph network of previous pixel line - (c) Shortest path between first and last element - (d) Final extracted, ordered data

3 Results

The results presented below were obtained from several XCT scans performed on the welded Al/Cu assemblies using the parameters shown in Table 1. They present a morphological description and quantification of an Al/Cu MPW interface.

3.1 Re-entrants features and vortexes

One of the advantages of XCT is its ability to detect interface morphologies that are not accessible using conventional topographic measurement techniques (e.g., mechanical or optical profilometers), such as interface shearing or re-entrant features [39]. This impossibility is linked to the measurement process itself and cannot be overcome currently, other techniques should be used.

Such features are very often present on MPW joints and are named "vortexes" ([32]), "waves" ([5]), "swirling" ([20]) or "wakes" in the literature. In this article, the terms "vortex"/"vortexes" designate re-entrant features, whereas the words "wave"/"waves" are reserved to describe the "hills" at the interface but without re-entrant features. Fig. 5 shows an example of a re-entrant feature which is later computed as an example on Fig. 7. Vortex detection was performed by measuring the gradient value of the ordered data on the x-axis. If the gradient had a positive value, elements were considered as "standard" whereas if the gradient had a negative value, elements were considered as members of a vortex. By taking the XYZ coordinate base

presented in Fig. 6 and the extracted data example in Fig. 7, it was possible to define a vortex feature as an ordered list of elements, as shown by squares 5, 6, and 7 in Fig. 7.

3.2 Vortex parameters

Different parameters such as the height and length were defined from the extracted vortexes. Several vortexes from different tomographic slices were gathered with respect to the proximity criterion. This criterion was based on the Euclidean distance between the vortex centers for each of the detected vortexes. The value of this criterion was flexible and could be modified according to the voxel size used during XCT.

The size of one detected vortex (the elements detected from Fig. 7) can be approximated as a right triangular surface (base $\times$ height divided by two). However, this approximation only compares the size of the re-entrant feature, it does not consider the possible "wave" portion (plateau on the top), which can be combined with the vortex. Table 3 shows the measurements obtained from different XCT on three samples (B, C, and D). Each sample was measured at three different locations, as shown in Fig. 6, at the beginning (Begin), middle (Center), and end (End) localization according to the welding direction. A vortex density was defined to normalize the number of vortexes per unit surface owing to the differences in the sample dimensions affecting the number of tomographic frames/pictures at different localizations.

3.3 Surface visualization

Once the XCT dataset was analyzed, the extracted interface lines were gathered and visualized to verify the quality of the process analysis and observe the global morphologies at the interface (an example is presented in Appendix A. Additional visualization of maps).

Appendix B. Supplementary data gathers additional visualizations for a data set. First one shows the interface evolution along the Y-axis, it is similar to the extracted pictures on Fig. 11 and Fig. 12. Second one displays a 3D view from a data set and its segmentation to reveal the wavy interface.

Fig. 8 shows the results obtained from the program. A clear morphological difference was observed between the Al/Cu and interface between air and copper (air/Cu). The interface with air represents the external surface of copper, which was polished during sample preparation. These maps provide sufficient information for a visual description of the morphology. The Al/Cu interface is heterogeneous along the X-axis, with waves on the left side and a flat area on the right side. The waves and vortexes are more homogeneous along the Y-axis, but they are not continuous along this direction. However, it is possible to visualize grooves on the raw polished surface using the SEPA 800 grit polishing paper used during the grinding step.

3.4 Height maps

Several height maps were obtained from the interface data. The standard height maps were defined using a unique coordinate triplet. One height value (Z-axis) was associated with a unique point on the grid plan (X-and Y axis). The extracted interface data containing the re-entrant features do not correspond to this description because of the

Samples	B			C			D		
Localization	Begin	Center	End	Begin	Center	End	Begin	Center	End
Number of pictures/frames (Y-axis)	366	421	401	566	561	511	436	431	416
Pixels used by length (X-axis)	1255	1280	1155	1240	1275	1235	1155	1290	1230
Number of vortexes	0	165	34	3	2044	352	9	1512	578
Number of vortexes groups	0	59	7	3	275	63	4	200	85
Surface area (mm^2)	1.31	1.54	1.32	2.00	2.04	1.80	1.44	1.59	1.46
Vortexes density ($vortex/mm^2$)	/	107	25.6	1.5	1002	195	6.3	952	395
Vortexes groups density ($vortex/mm^2$)	/	38.3	5.3	1.5	135	35.0	2.8	126	58.2
Average vortexes size (μm^2)	/	9.1	11.1	4.7	7.6	11.7	4.1	12.4	18.3

Table 3: Extracted vortex parameters for different sections and localizations of different welding samples

multiple-height solutions for a unique position on the grid. Three height maps were defined to avoid this issue: minimum, average, and maximum. For multiple heights at a unique location, the map presents the minimum, mean, or maximum of the multiple pixels at this location. Fig. 9 shows the local variations that could be created depending on the chosen map.

Local variations caused by distinct maps can have a slight impact on the measurements of the surface parameters obtained using these maps. However, the hill/wave features do not affect the maps, and the presence of re-entrant features/vortexes is limited to the interface surface. For instance, in sample D, localized at the End from Table 3, there are 11 672 voxels that are involved for multiple locations, and these voxels represent only 2.3% of the final surface.

3.5 Topographic surface parameters

Height maps can be exported and analyzed using specialized software (such as Mountains [8]) to obtain the texture surface parameters. Following ISO 25178-2 [13], the parameters are measured using different surface height maps. Table 4 shows these results for one localization of one sample as an example. During this work, the different

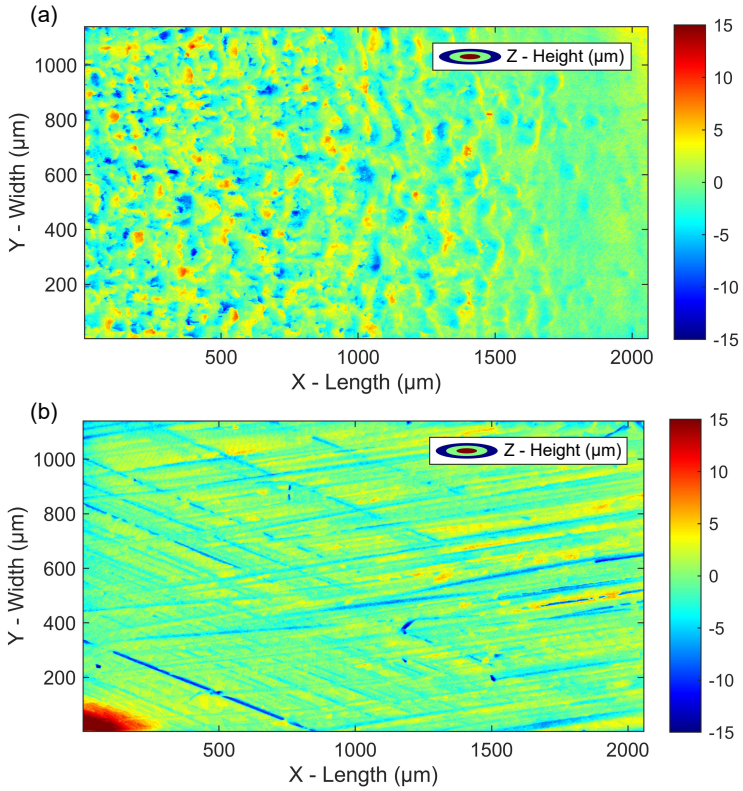

Figure 8: Topographic maps of interface after process analysis of XCT data - (a) Al/Cu interface topographic map located near welding zone end - (b) Air/Cu interface topographic map after grinding during sample preparation

surfaces followed the same procedure, a third-degree polynomial was applied to remove the global shape of the sample and an L-filter (second order Robust Gaussian Filter) of 0.25 mm was executed on the samples. Finally, the roughness parameters (also called topographic parameters) were calculated on the filtered surfaces.

As previously indicated, the texture surface parameters results for different height maps are discussed in section 4. Discussion. Table 5 shows the same texture surface parameters albeit calculated for the different localizations (Begin, Center, and End) of sample B. The roughness parameters computed from the average height maps of the different samples and their localizations are depicted in Figure 10. The same trends and variations were observed in the different samples (B, C, and D).

Additional parameters such as the Std (texture direction of the surface) or the Vvv (valley void volume) can be extracted to describe the surface for a specific study, however, they are less commonly used or are not relevant for this study. In addition, it is important to note that the surface motifs are not homogeneous. A gradient exists

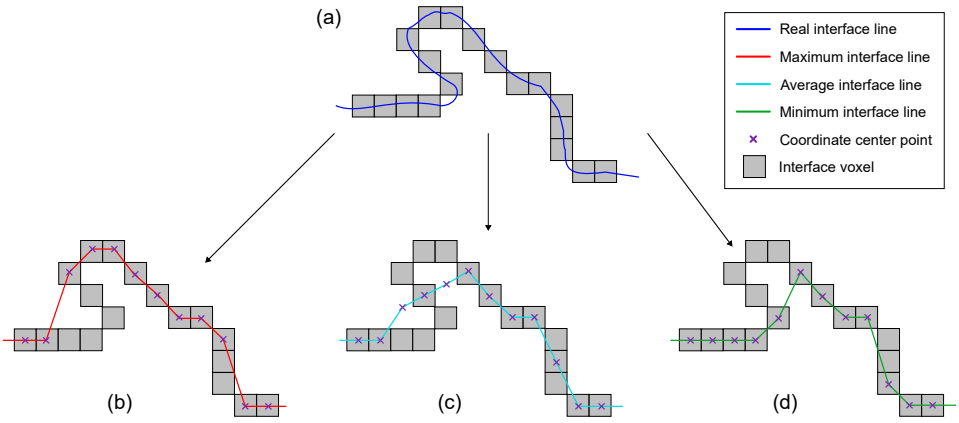

Figure 9: Scheme for variations in different height maps for vortex composed of interface voxels - (a) Real interface line with interface voxel - (b) Maximum interface line for maximum height map - (c) Mean interface line for average height map - (d) Minimum interface line for minimum height map

Parameter	Sample D - End localization		
Height map used	Minimum	Average	Maximum
Sa - µm	2.013	2.025	2.065
Sq - µm	2.686	2.687	2.777
Ssk	-0.4386	-0.4742	-0.6732
Sku	4.558	4.407	5.069
Sdr - %	20.49	20.71	21.49

Table 4: Texture surface parameter comparison for sample D localized at End with three different types of height maps described

Parameter	Sample B - Average map		
Localization	Begin	Center	End
Sa - µm	0.7341	1.560	1.393
Sq - µm	1.148	2.079	1.895
Ssk	-0.2464	-0.2624	-0.3861
Sku	4.293	3.909	4.494
Sdr - %	13.14	29.22	14.86

Table 5: Texture surface parameter comparison for sample B with average height maps and different localization

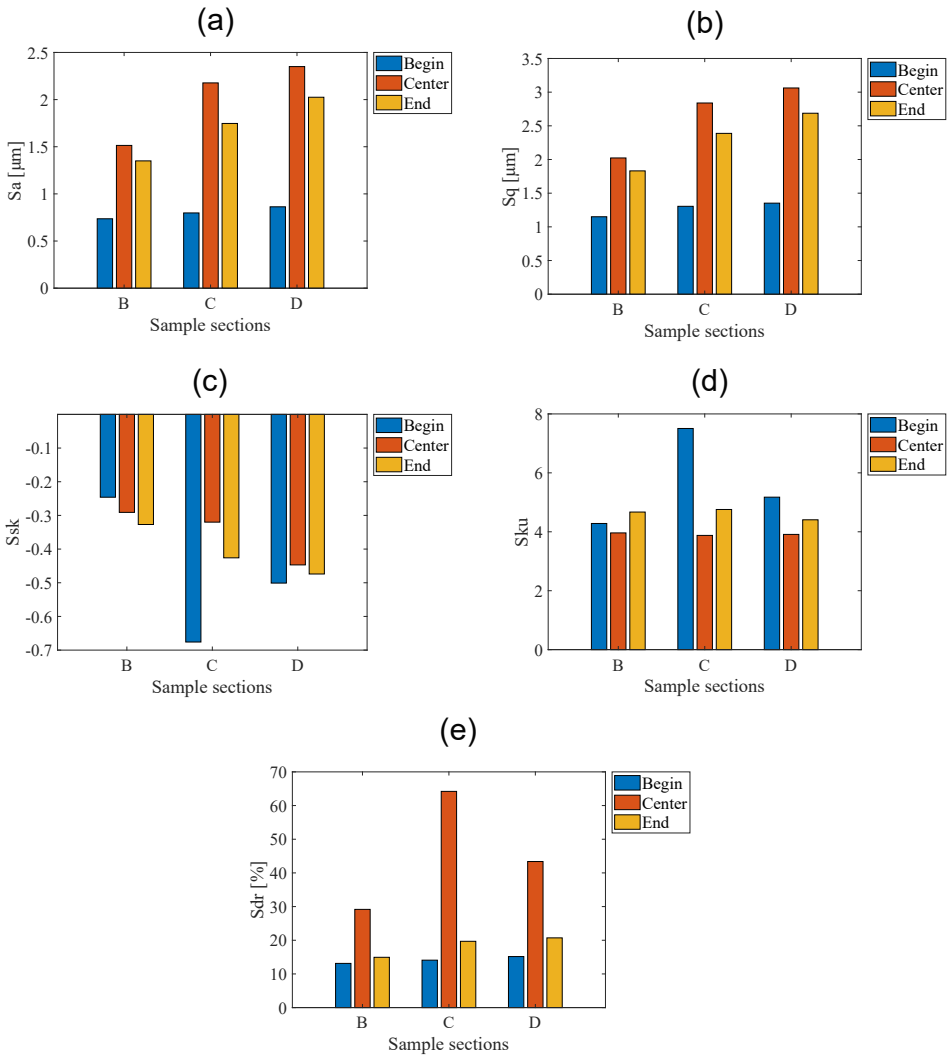

Figure 10: Plot of roughness parameters for different samples (B, C, and D) and localization (Begin, Center, End) for average height map - (a) Sa measurements - (b) Sq measurements - (c) Ssk measurements - (d) Sku measurements - (e) Sdr measurements

along the X-axis (see Fig. 8(a)) and is linked to the transition regime of the MPW process.

3.6 Vortex morphology

Vortexes are generally studied only on the perpendicular cross section of the weld, thus providing 2D information, whereas vortexes can be described as a 3D phenomenon.

XCT can produce this additional information (in the third dimension) by investigating the previous and subsequent sections of a detected vortex to evaluate its evolution on the lateral sides (Y-axis). Two different vortex morphologies are observed.

3.6.1 Standard vortex

A standard vortex is the first type of identified vortex. This can be described as a standard wave with a swirl at its end. This description corresponds to the elements shown in Fig. 5. This type of vortex is important because it expands the surface area between the two welding elements, owing to the augmented contact area from the vortex curvature.

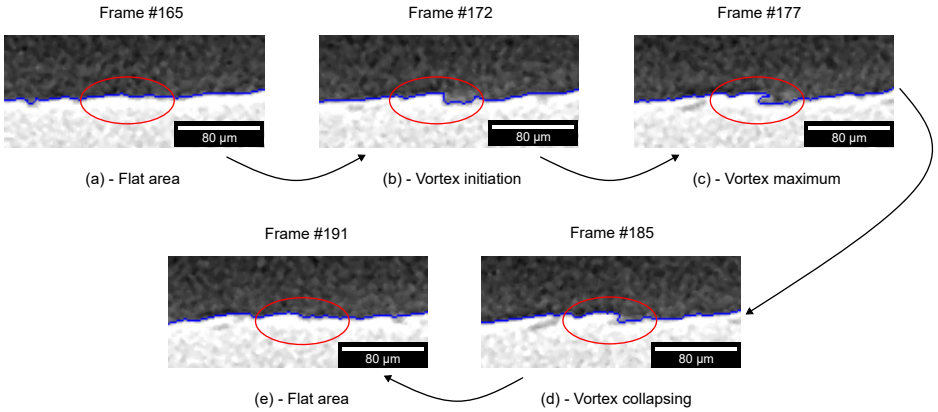

Figure 11: Standard vortex morphology evolution on width (Y-axis)

Fig. 11 presents the standard vortex morphology evolution along different tomographic sections. Vortex growth and crumbling are gradual in the snapshots. By taking the different slices, this vortex measures approximately 10 µm height, 8 µm length and 45 µm width. This indicates that the vortexes are not necessarily continuous along the width direction (the Y-axis corresponds to the evolution of the frame number).

3.6.2 Broken vortex

The second type of vortex that is detected is the broken vortex. This type of vortex corresponds to an elongated vortex in the length direction (X-axis) or a vortex swirling on itself that can contain an intermetallic compound (IMC) pocket or cavity. Intermetallic compounds can be formed as a result of localized high-pressure and elevated temperatures at the interface. Examples of such pockets and cavities were observed experimentally [28] and reproduced numerically [19] for tube welding. However, this vortex type possesses areas where the elongated section is broken at the center and separated into two.

Fig. 12 shows the creation and evolution of this vortex type along the width direction. Initially (Frame 24), the broken vortex is designed as a wave in the figure

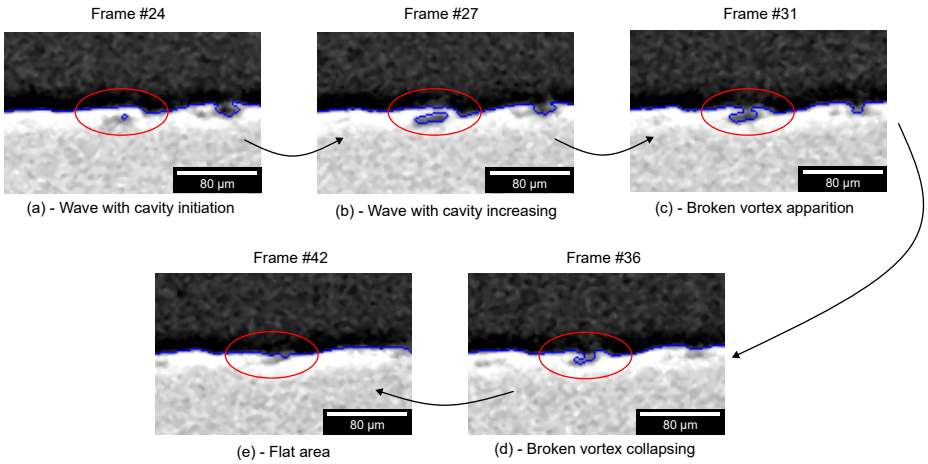

Figure 12: Broken vortex morphology evolution on width (Y-axis)

because of the absence of a negative gradient at this stage of the process, following the nomenclature presented in subsection 3.1. Re-entrants features and vortexes. The middle cavity probably corresponds to an IMC pocket at the center of this broken vortex. Frame 31 shows the breaking of the vortex into two arms (right and left) before their collapse in frame 36. Frame 42 illustrates the interface returning to a flat surface.

It is possible to automate the labeling of the two vortex types. The left and right arms exhibit negative gradients. Therefore, they can be classified as vortexes. However, the distance between them is limited, compared with the distance between two consecutive standard vortexes on the same tomographic frame. A distance criterion based on Euclidean distance was used to segment the vortex types. In this study, the distance criterion was set to 34 µm. This choice was based on the histogram of the differences of the vortex locations and the visual observation of the morphology size. The measured distance between the two arms from frame 31 of Fig. 12 is 25 µm, which explains the categorization of this vortex as a broken vortex because of the double arms.

4 Discussion

4.1 Method and program efficiency

The method developed in this study permits the automated treatment of the data from the XCT. The associated routine is used to extract the interfacial surface between two dissimilar materials. Automated segmentation performs better than manual segmentation. Furthermore, this selection is not biased by any human selection of the segmentation value. Thus, the execution speed can be considered correct. The program can generate a tomographic picture dataset of 500 Mo in less than five minutes using a laptop computer equipped with 32 Go RAM memory and an i7-10875H CPU. The calculation time includes the continuous display of the processed data to ensure correct

segmentation at the interface. The longest execution period, which was approximately 20% of the total time (1 min), corresponds to the graph network reconstruction of the interface presented in Fig. 7.

The program is highly dependent on the input image quality. For blurred images or images with strong X-ray artifacts, the interface demarcation is unclear, and the vortexes are not captured correctly. Small artificial vortexes can be created at the interface, and the surface reconstruction contains additional high-frequency noise. This noise problem affects the C-Center dataset, and is visible in Table 3. The number of vortexes detected is slightly lower than that presented herein. However, the shape of the main morphology is maintained. Quality analysis can be performed on the back surface of the samples (air/Cu interface) to evaluate the data quality. The back surface does not contain vortexes. For sample C, the air/Cu interface of localizations C-Begin and C-End yields 0 and 2 vortexes, respectively, whereas for C-Center, approximately 1000 vortexes were detected. The back surfaces (air/Cu interface) of C-Begin, C-Center, and C-End are physically the same because they were produced by the same grinding step (as shown in Fig. 8); therefore, they should obtain the same order of magnitude of detected vortexes. This demonstrates the impact of the data quality on the results. Note that the contrast difference between the two materials or phases should be sufficient to obtain a clear interfacial line between them.

4.2 Surface and vortex parameters

The vortex distribution was inhomogeneous along the welding seam, and evolution occurred along the X and Y-axes. Table 3 shows the evolution of the vortex density along the different samples (B, C, D) and their respective localization (Begin, Center, End). No direct correlation was observed between the number of vortexes and their sizes. For a given sample, vortexes appeared at the center of the weld with a limited size and grew along the X-axis, but their numbers were reduced. Thus, fewer vortexes were present in the end localization, but their average size was larger.

On the lateral side of the weld (along the Y-axis), the size effect was limited between the different samples. An evolution in the density was observed. The external side of the weld (sample B) had fewer vortexes than the inner side (sample D) along the Y-axis. Sample C followed the same trend (except for sample C-Center, as previously explained). Note that large vortexes are easier to detect than small vortexes.

The roughness parameters also demonstrate the evolution of the surface morphology along different localizations (Beginning, Center, and End) for a determined sample (see Table 5). This evolution can be considered reliable because of the stability of the surface parameters at a single location. Table 4 demonstrates that arithmetical mean height (Sa) and root mean square height (Sq) are almost totally independent of the height map chosen. This was not the case for Skewness (Ssk), Kurtosis (Sku), and Surface Development Ratio (Sdr), which were slightly affected by the map choice, particularly for the maximum height maps. This is directly linked to the types of surfaces investigated in this study. The height distribution of the surfaces was not symmetrical around the mean plane (as indicated by a Ssk inferior to 0). Most of the vortexes and waves were above the mean plane. This implies that choosing the maximum height

map increases the difference by choosing the highest point for multiple possibilities (see Fig. 9).

The roughness parameters followed the same trends as those extracted from the vortexes. The Begin localization surfaces are flatter with less variation than those of the Center and End localization surfaces for the different samples (see Fig. 10).

The Sdr represents the ratio of the measured surface shape area to the flat surface area as a percentage. This shows that several small vortexes at the Center develop a larger contact surface area between the two dissimilar surfaces than those of the larger vortexes (but less abundant), such as those located at the End interface. Once again, the inner welding sections (C and D) have a higher Sdr than that of the external section B at the three locations (Begin, Center, and End).

The Sku parameter indicates sharp morphologies for all the studied surfaces.

It can be difficult to precisely link the evaluation of these roughness parameters to the precise surface morphology. Several criteria must be considered to understand vortex-type morphology and localization.

4.3 Vortexes and wave evolution

As previously mentioned, the waves and vortexes evolved along the welding direction (X-axis) and width (Y-axis). Fig. 13 exposes the variation of the global morphologies on the surface for sample D with these different localizations. The waves and vortexes evolve from small rounded hills to elongated shapes with an orientation perpendicular to the welding direction. They increase in height before disappearing from the welding end.

The results show that the interface condition is not stable for both axes at the beginning of welding (Begin localization for samples B, C, and D). The process conditions then evolve to be stable in width (Y-axis, perpendicular to the welding direction), and thus create specific elongated waves and vortexes of the MPW.

By considering previous works ([6, 11]), a hypothesis can be made to explain broken vortex creation from the wave formation mechanisms. Broken vortexes can be seen as unstable vortexes owing to an excessive shearing deformation at the top of the wave until it reaches its mechanical limit; the vortex undergoes necking, and a rupture appears. The released broken part can interact with the interface element and produce different intermetallic compounds or act as an obstacle during the creation of the welding seam.

Fig. 14 shows an optical image from an Al/Cu welded joint interface produced under the same process conditions. Features similar to the broken vortexes found during the X-ray analysis are visible. These areas also correspond to intermetallic pockets with different chemical compositions (light and dark grays). There is a feature link between the morphologies that have been found in the XCT analysis and the optical images. Note that a version of the program can be used with optical or electronic images (gray or color) to separate two dissimilar phases along an interface. The same vortex properties are extracted from this type of image.

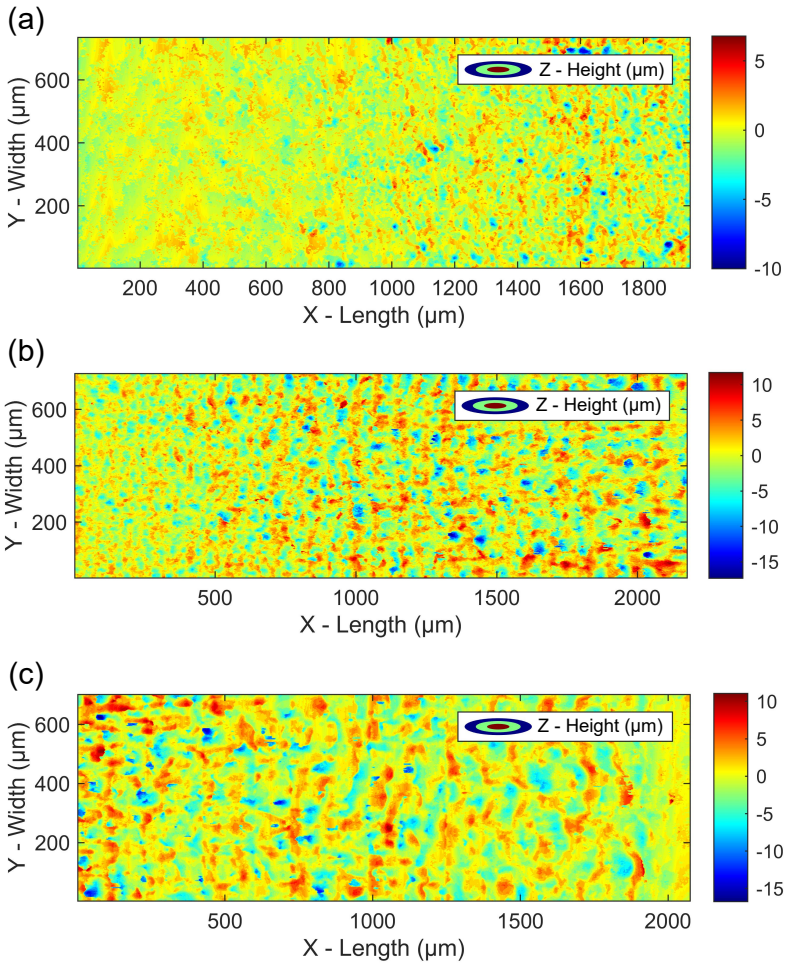

Figure 13: Maximum height maps for Al/Cu interface of sample D - (a) Begin of welding - (b) Center of welding - (c) End of welding

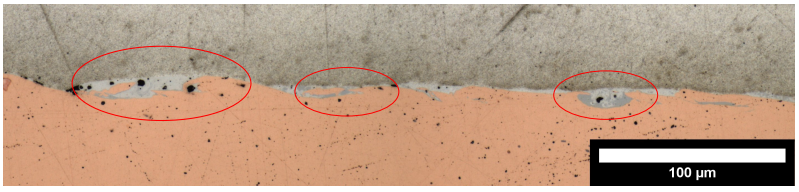

Figure 14: Stitched optical image from Al/Cu welded joint interface with highlighted broken vortex features at different stages

5 Conclusion

A specific program was developed based on a new approach to extract and analyze the interface surface between two dissimilar materials from XCT data. This method was successfully applied to Al/Cu assemblies produced using MPW; it led to the identification of two vortex morphologies at the welding interface: standard and broken. The morphology of these vortexes is also described and a connection with the process conditions during the MPW welding is proposed.

The method also enabled the investigation on quantitative measurements such as the feature sizes. This size evolution was evaluated along both the welding direction and width. The study showed that the distribution of vortexes and waves is not uniform along the welding direction, and there is a progressive increase in their dimensions. The average surface of the vortexes can triple between the beginning and end of the welding. Waves and vortexes are not stable on the welding width and collapse regularly. This allows to demonstrate the interlocking between the two materials.

Several types of surfaces were extracted from one area and analyzed with topography software to obtain roughness parameters and compare the surfaces using these metrics. The results of our study describe up to a doubling of the surface roughness between the two components. The surface area between the two materials increased by more than 26% on average.

The proposed method can be readily used in practice to measure surface parameters and vortexes depending on the process conditions used during welding. Produced surfaces can be exported in .stl files to be later used in mechanical modeling and simulation to compare the expected interface in simulation with the experimental one. Further studies can also be performed using this method to locally correlate the joint strength during mechanical tests (experimental or simulation) with the developed surface area or interlocking morphology.

Supplementary information. This article contains supplementary files.

Acknowledgments. The authors would like to thank the ISIS4D X-ray CT regional platform funded by the International Campus on Safety and Intermodality in Transportation (CISIT), the Hauts-de-France Région, the European Community and the National Center for Scientific Research for the use of their tomographic equipment, and M. Jérome Hosdez for the production of the scan. The authors acknowledge PFT Innovaltech for supplying the Al/Cu samples welded by MPW.

Declarations

Funding

The authors did not receive support from any organization for the submitted work.

Competing Interests

The authors have no relevant financial or non-financial interests to disclose.

Data availability

The datasets generated during and/or analyzed during the current study are available from the corresponding author on reasonable request.

CRediT author statement

- Benjamin Zielinski : Conceptualization, Methodology, Software, Validation, Investigation, Data Curation, Writing - Original Draft, Visualization
- Tarik Sadat : Conceptualization, Methodology, Validation, Writing - Review & Editing
- Robin Guibert : Methodology, Software, Writing - Review & Editing
- Denis Jouaffre : Ressources
- Eric Markiewicz : Conceptualization, Supervision, Project administration, Funding acquisition
- Laurent Dubar : Conceptualization, Supervision, Project administration, Funding acquisition

Consent to participate

Not applicable

Appendix A Additional visualization of maps

This appendix presents additional height maps visualizations for Sample-D-End, which can be computed using an in-house program. Fig. A1 shows a visualization for the raw extracted line from the tomographic section. It has the advantage of visualizing vortexes that are not visible on standard height maps.

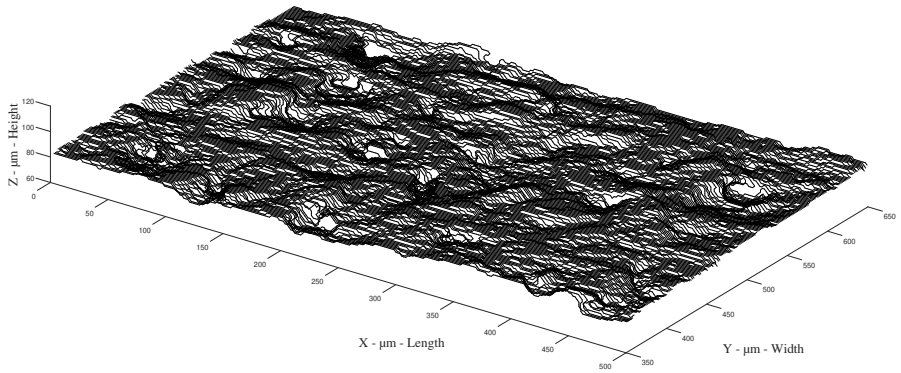

Figure A1: Local line-plot from tomographic section to visualize Al/Cu interface - Sample D - End localization

Fig. A2 depicts the full Al/Cu interface of sample D-End with a 3D-view. This provides a general overview of the surface. However, only one type of height map must be chosen from the minimum, mean, and maximum maps.

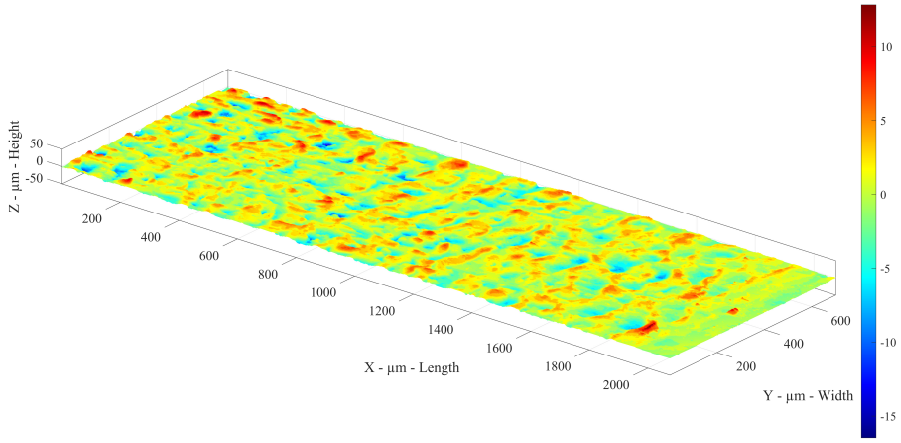

Figure A2: 3D plot for mean height map on full sample - Sample D - End localization

Fig. A3 corresponds to the same area displayed on Fig. A1 albeit with a standard visualization. The figure shows that vortexes are easier to identify with a plot-line visualization, but the standard view permits a better understanding and global insight.

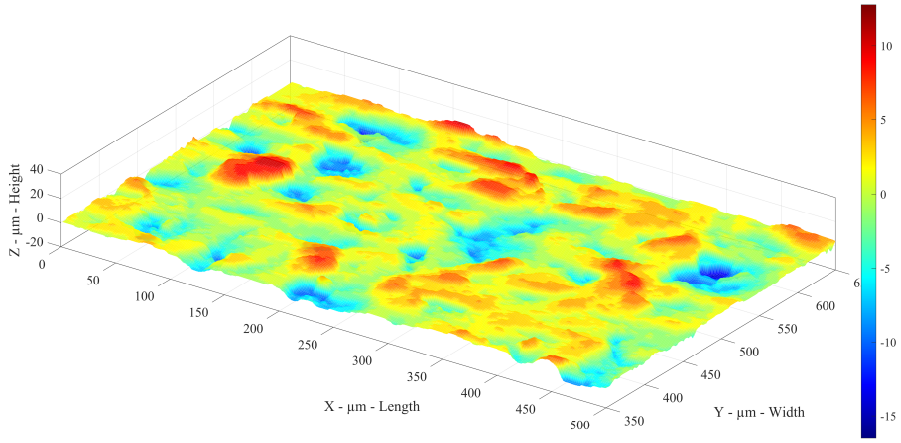

Figure A3: 3D plot for mean height map on local area - Sample D - End localization

Appendix B Supplementary data

Additional visualizations for a data set.

First one (.gif) allows to follow the waves and vortexes morphological evolution at the interface. Second one (video) allows to get a 3D view from the tomographic data and to visualize the wavy interface between the two materials. It has been realized by using Dragonfly software (Object Research Systems).

References

[1] Aizawa Y, Nishiwaki J, Harada Y, et al (2016) Experimental and numerical analysis of the formation behavior of intermediate layers at explosive welded Al/Fe joint interfaces. Journal of Manufacturing Processes 24:100–106. https://doi.org/10.1016/j.jmapro.2016.08.002, URL http://dx.doi.org/10.1016/j.jmapro.2016.08.002

[2] Ajmi C, Zapata J, Martínez-Álvarez JJ, et al (2020) Using Deep Learning for Defect Classification on a Small Weld X-ray Image Dataset. Journal of Nondestructive Evaluation 39(3):1–13. https://doi.org/10.1007/s10921-020-00719-9, URL https://doi.org/10.1007/s10921-020-00719-9

[3] Antonini JM (2003) Health effects of welding. Critical Reviews in Toxicology 33(1):61–103. https://doi.org/10.1080/713611032

[4] Avettand-Fènoël MN, Sapanathan T, Pirling T, et al (2021) Investigation of residual stresses in planar dissimilar magnetic pulse welds by neutron diffraction. Journal of Manufacturing Processes 68(April):1758–1766. https://doi.org/10.1016/j.jmapro.2021.06.071

[5] Ben-Artzy A, Stern A, Frage N, et al (2008) Interface phenomena in aluminium-magnesium magnetic pulse welding. Science and Technology of Welding and Joining 13(4):402–408. https://doi.org/10.1179/174329308X300136

[6] Ben-Artzy A, Stern A, Frage N, et al (2010) Wave formation mechanism in magnetic pulse welding. International Journal of Impact Engineering 37(4):397–404. https://doi.org/10.1016/j.ijimpeng.2009.07.008, URL http://dx.doi.org/10.1016/j.ijimpeng.2009.07.008

[7] Díaz FV, Peralta ME, Fernandino DO (2021) Study of Sphericity and Compactness Parameters in Spheroidal Graphite Iron Using X-Ray Micro-computed Tomography and Image Processing. Journal of Nondestructive Evaluation 40(1):1–10. https://doi.org/10.1007/s10921-020-00738-6, URL https://doi.org/10.1007/s10921-020-00738-6

[8] Digital Surf (2022) Digital Surf - Mountains software. URL https://www.digitalsurf.com/

[9] Gleason G, Bailey K, Sunny S, et al (2022) Influence of surface roughness on the transient interfacial phenomena in laser impact welding. Journal of Manufacturing Processes 80(February):480–490. https://doi.org/10.1016/j.jmapro.2022.06.022, URL https://doi.org/10.1016/j.jmapro.2022.06.022

[10] Gu C, Lu Y, Luo AA (2021) Three-dimensional visualization and quantification of microporosity in aluminum castings by X-ray micro-computed tomography. Journal of Materials Science and Technology 65:99–107. https://doi.org/10.1016/j.jmst.2020.03.088, URL https://doi.org/10.1016/j.jmst.2020.03.088

[11] Gupta V, Lee T, Vivek A, et al (2019) A robust process-structure model for predicting the joint interface structure in impact welding. Journal of Materials Processing Technology 264(March 2018):107–118. https://doi.org/10.1016/j.jmatprotec.2018.08.047, URL https://doi.org/10.1016/j.jmatprotec.2018.08.047

[12] Hahn M, Weddeling C, Taber G, et al (2016) Vaporizing foil actuator welding as a competing technology to magnetic pulse welding. Journal of Materials Processing Technology 230:8–20. https://doi.org/10.1016/j.jmatprotec.2015.11.010

[13] ISO (2012) 25178:2 - Geometrical product specifications (GPS) — Surface texture: Areal — Part 2: Terms, definitions and surface texture parameters, URL https://www.iso.org/standard/42785.html

[14] Kapil A, Sharma A (2015) Magnetic pulse welding: An efficient and environmentally friendly multi-material joining technique. Journal of Cleaner Production 100:35–58. https://doi.org/10.1016/j.jclepro.2015.03.042, URL http://dx.doi.org/10.1016/j.jclepro.2015.03.042

[15] Lee T, Zhang S, Vivek A, et al (2019) Wave formation in impact welding: Study of the Cu–Ti system. CIRP Annals 68(1):261–264. https://doi.org/10.1016/j.cirp.2019.04.058, URL https://doi.org/10.1016/j.cirp.2019.04.058

[16] Lee T, Nassiri A, Dittrich T, et al (2020) Microstructure development in impact welding of a model system. Scripta Materialia 178:203–206. https://doi.org/10.1016/j.scriptamat.2019.11.031

[17] Li C, Zhou Y, Shi X, et al (2020) Magnetic field edge-effect affecting joint macro-morphology in sheet electromagnetic pulse welding. Materials and Manufacturing Processes 35(9):1040–1050. https://doi.org/10.1080/10426914.2020.1758332, URL https://doi.org/10.1080/10426914.2020.1758332

[18] Li J, Vivek A, Daehn G (2021) Improved properties and thermal stability of a titanium-stainless steel solid-state weld with a niobium interlayer. Journal of Materials Science and Technology 79:191–204. https://doi.org/10.1016/j.jmst.2020.11.050, URL https://doi.org/10.1016/j.jmst.2020.11.050

[19] Li JS, Raoelison RN, Sapanathan T, et al (2020) Interface evolution during magnetic pulse welding under extremely high strain rate collision: mechanisms, thermomechanical kinetics and consequences. Acta Materialia 195:404–415. https://doi.org/10.1016/j.actamat.2020.05.028

[20] Li JS, Sapanathan T, Raoelison RN, et al (2021) On the complete interface development of Al / Cu magnetic pulse welding via experimental characterizations and multiphysics numerical simulations. Journal of Materials Processing Technology 296(April). https://doi.org/10.1016/j.jmatprotec.2021.117185

[21] Lu Z, Gong W, Chen S, et al (2019) Interfacial microstructure and local bonding strength of magnetic pulse welding joint between commercially pure aluminum 1060 and AISI 304 stainless steel. Journal of Manufacturing Processes 46(December 2018):59–66. https://doi.org/10.1016/j.jmapro.2019.07.041, URL https://doi.org/10.1016/j.jmapro.2019.07.041

[22] Meng Z, Gong M, Guo W, et al (2020) Numerical simulation of the joining interface of dissimilar metals in vaporizing foil actuator welding: Forming mechanism and factors. Journal of Manufacturing Processes 60(July):654–665. https://doi.org/10.1016/j.jmapro.2020.11.009, URL https://doi.org/10.1016/j.jmapro.2020.11.009

[23] Mousavi AA, Al-Hassani ST (2005) Numerical and experimental studies of the mechanism of the wavy interface formations in explosive/impact welding. Journal of the Mechanics and Physics of Solids 53(11):2501–2528. https://doi.org/10.1016/j.jmps.2005.06.001

[24] Nassiri A, Abke T, Daehn G (2019) Investigation of melting phenomena in solid-state welding processes. Scripta Materialia 168:61–66. https://doi.org/10.1016/j.scriptamat.2019.04.021, URL https://doi.org/10.1016/j.scriptamat.2019.04.021

[25] Otsu N (1979) A threshold selection method from gray-level histograms. IEEE transactions on systems, man, and cybernetics 9(1):62–66

[26] Raoelison RN, Buiron N, Rachik M, et al (2012) Efficient welding conditions in magnetic pulse welding process. Journal of Manufacturing Processes 14(3):372–377. https://doi.org/10.1016/j.jmapro.2012.04.001, URL http://dx.doi.org/10.1016/j.jmapro.2012.04.001

[27] Raoelison RN, Racine D, Zhang Z, et al (2014) Magnetic pulse welding: Interface of Al/Cu joint and investigation of intermetallic formation effect on the weld features. Journal of Manufacturing Processes 16(4):427–434. https://doi.org/10.1016/j.jmapro.2014.05.002, URL http://dx.doi.org/10.1016/j.jmapro.2014.05.002

[28] Raoelison RN, Sapanathan T, Buiron N, et al (2015) Magnetic pulse welding of Al/Al and Al/Cu metal pairs: Consequences of the dissimilar combination on the interfacial behavior during the welding process. Journal of Manufacturing Processes 20:112–127. https://doi.org/10.1016/j.jmapro.2015.09.003, URL http://dx.doi.org/10.1016/j.jmapro.2015.09.003

[29] Song JW, Park JJ, Lee GJ, et al (2020) Effect of Impact Velocity on Interface Characteristics of HT-9 Steel Joints Fabricated by Magnetic Pulse

Welding. Metals and Materials International 26(3):360–369. https://doi.org/10.1007/s12540-019-00510-0, URL https://doi.org/10.1007/s12540-019-00510-0

[30] Townsend A, Pagani L, Scott P, et al (2017) Areal surface texture data extraction from X-ray computed tomography reconstructions of metal additively manufactured parts. Precision Engineering 48:254–264. https://doi.org/10.1016/j.precisioneng.2016.12.008, URL http://dx.doi.org/10.1016/j.precisioneng.2016.12.008

[31] Townsend A, Racasan R, Leach R, et al (2018) An interlaboratory comparison of X-ray computed tomography measurement for texture and dimensional characterisation of additively manufactured parts. Additive Manufacturing 23(July):422–432. https://doi.org/10.1016/j.addma.2018.08.013, URL https://doi.org/10.1016/j.addma.2018.08.013

[32] Wang P, Chen D, Yan Y, et al (2021) Hierarchical morphology and formation mechanism of collision surface of al/steel dissimilar lap joints via electromagnetic pulse welding. Metals 11(9). https://doi.org/10.3390/met11091468

[33] Wang PQ, Chen DL, Ran Y, et al (2020) Electromagnetic pulse welding of Al/Cu dissimilar materials: Microstructure and tensile properties. Materials Science and Engineering A 792(April):139842. https://doi.org/10.1016/j.msea.2020.139842, URL https://doi.org/10.1016/j.msea.2020.139842

[34] Wang S, Xu L, Sun T, et al (2021) Effects of process parameters on mechanical performance and interfacial morphology of electromagnetic pulse welded joints between aluminum and galvanized steel. Journal of Materials Research and Technology 10:552–564. https://doi.org/10.1016/j.jmrt.2020.12.047, URL https://doi.org/10.1016/j.jmrt.2020.12.047

[35] Wei Y, Li H, Xiao P, et al (2020) Microstructure and Conductivity of the Al-Cu Joint Processed by Friction Stir Welding. Advances in Materials Science and Engineering 2020. https://doi.org/10.1155/2020/6845468

[36] Xu Z, Cui J, Yu H, et al (2013) Research on the impact velocity of magnetic impulse welding of pipe fitting. Materials and Design 49:736–745. https://doi.org/10.1016/j.matdes.2012.12.059, URL http://dx.doi.org/10.1016/j.matdes.2012.12.059

[37] Zanini F, Sbettega E, Sorgato M, et al (2019) New Approach for Verifying the Accuracy of X-ray Computed Tomography Measurements of Surface Topographies in Additively Manufactured Metal Parts. Journal of Nondestructive Evaluation 38(1):1–10. https://doi.org/10.1007/s10921-018-0547-4, URL https://doi.org/10.1007/s10921-018-0547-4

[38] Zhang C, Song C, Zhu W, et al (2022) Interfaces of the 5083Al/1060Al/TA1/Ni/SUS304 five-layer composite plate fabricated by explosive welding. Journal of Materials Research and Technology 19:314–331. https://doi.org/10.1016/j.jmrt.2022.04.157, URL https://doi.org/10.1016/j.jmrt.2022.04.157

[39] Zhang F, Liu J, Ding X, et al (2020) A discussion on the capability of X-ray computed tomography for contact mechanics investigations. Tribology International 145(December 2019):106167. https://doi.org/10.1016/j.triboint.2020.106167, URL https://doi.org/10.1016/j.triboint.2020.106167

[40] Zhang H, Yang Z, Ren L (2019) Experimental investigation on structure parameters of E-shaped coil in magnetic pulse welding. Materials and Manufacturing Processes 34(15):1701–1709. https://doi.org/10.1080/10426914.2019.1689263, URL https://doi.org/10.1080/10426914.2019.1689263

[41] Zhang K, Meng Q, Zhang X, et al (2022) Quantitative characterization of defects in stereolithographic additive manufactured ceramic using X-ray computed tomography. Journal of Materials Science and Technology 118:144–157. https://doi.org/10.1016/j.jmst.2021.11.060, URL https://doi.org/10.1016/j.jmst.2021.11.060

[42] Zhang Y, Babu SS, Daehn GS (2010) Interfacial ultrafine-grained structures on aluminum alloy 6061 joint and copper alloy 110 joint fabricated by magnetic pulse welding. Journal of Materials Science 45(17):4645–4651. https://doi.org/10.1007/s10853-010-4676-0

[43] Zhou Y, Li C, Shi X, et al (2022) Evaluation model of electromagnetic pulse welding effect based on Vc-β trajectory curve. Journal of Materials Research and Technology 20(Imc):616–626. https://doi.org/10.1016/j.jmrt.2022.07.069, URL https://doi.org/10.1016/j.jmrt.2022.07.069

[44] Zielinski B, Sadat T, Lukić B, et al (2023) Characterization of local mechanical properties of Al/Cu Magnetic Pulse Welded joints under high strain rates using synchrotron X-ray imaging. Materials Letters 337(November 2022). https://doi.org/10.1016/j.matlet.2023.133943